Granular Matter

Stress-dilatancy behavior of fouled ballast: Experiments and DEM modelling

--Manuscript Draft--

Manuscript Number:	
Full Title:	Stress-dilatancy behavior of fouled ballast: Experiments and DEM modelling
Article Type:	Original Report
Keywords:	Stress-dilatancy relationship, Fouling, coal, clay fines, Direct shear test, Discrete element method
Corresponding Author:	J.S. Vinod University of Wollongong AUSTRALIA
Corresponding Author Secondary Information:	
Corresponding Author's Institution:	University of Wollongong
Corresponding Author's Secondary Institution:	
First Author:	Jing Chen
First Author Secondary Information:	
Order of Authors:	Jing Chen
	Buddhima Indraratna, PhD, FTSE, FIEAust, FASCE, FGS, FAusIMM, FIES, DIC
	J.S. Vinod, PhD
	Trung Ngo, PhD
	Rui Gao, PhD
	Yangzepeng Liu
Order of Authors Secondary Information:	
Funding Information:	Chinese Government Scholarship (201906270149) — Ms Jing Chen
	ARC Industrial Transformation Training Centre, ITTC-Rail (IC170100006) — D/Prof. Buddhima Indraratna
	National Natural Science Foundation of China (51878521,51178358) — Prof. Rui Gao
Abstract:	This paper presents a study of the mechanical behavior of ballast contaminated by different fouling agents such as coal and subgrade clay. Large-scale direct shear tests were carried out to examine the strength and deformation properties for coal-fouled and clay-fouled ballast. The experimental results show that fouled ballast (both clay and coal) exhibits a lower peak shear strength and decreased dilation during shearing. The clay-fouled ballast shows higher shear strength and smaller dilation compared to coal-fouled ballast. The relationship between shear stress and dilatancy of ballast under different fouling conditions is reported in this paper, where the numerical predictions are made using the discrete element method (DEM). The DEM simulations show that with the increase of fouling level, the coordination number, the average contact force, the particle rotation and the velocity decreases for ballast aggregates. The results indicate that coal-fouled ballast exhibits a smaller average contact forces with less stress concentrations, less major principal stress orientation and a greater coordination number, leading to less particle rotation and velocity compared to those of clay-fouled ballast for the same degree of fouling.
Suggested Reviewers:	
Requested Editor:	

Stress-dilatancy behavior of fouled ballast: Experiments and DEM modelling

Jing Chen[a,b], Buddhima Indraratna[c], Jayan S. Vinod[b,*] Trung Ngo[c], Rui Gao[a], Yangzepeng Liu[a]

[a]*School of Civil Engineering, Wuhan University, Wuhan 430072, China*

[b]*Faculty of Engineering and Information Sciences, Univeristy of Wollongong, Wollongong City, NSW 2522, Australia*

[c]*Transportation Research Centre, Faculty of Engineering and Information Technology, University of Technology Sydney, Sydney, NSW 2007, Australia*

ABSTRACT: This paper presents a study of the mechanical behavior of ballast contaminated by different fouling agents such as coal and subgrade clay. Large-scale direct shear tests were carried out to examine the strength and deformation properties for coal-fouled and clay-fouled ballast. The experimental results show that fouled ballast (both clay and coal) exhibits a lower peak shear strength and decreased dilation during shearing. The clay-fouled ballast shows higher shear strength and smaller dilation compared to coal-fouled ballast. The relationship between shear stress and dilatancy of ballast under different fouling conditions is reported in this paper, where the numerical predictions are made using the discrete element method (DEM). The DEM simulations show that with the increase of fouling level, the coordination number, the average contact force, the particle rotation and the velocity decreases for ballast aggregates. The results indicate that coal-fouled ballast exhibits a smaller average contact forces with less stress concentrations, less major principal stress orientation and a greater coordination number, leading to less particle rotation and velocity compared to those of clay-fouled ballast for the same degree of fouling.

Keywords: Stress-dilatancy relationship, Fouling, coal, clay fines, Direct shear test, Discrete element method

1. Introduction

Ballasted railways are among the most common transportation modes worldwide. Compared to air freight or ocean shipping, railways have their superiority in heavy-haul capacity, low operating cost and high efficiency especially for long-distance inland transportation. However, ballast fouling is a critical problem in railway systems as it is often considered as a major contributing hazardous track

conditions, such as differential settlement, impeded drainage and reduced bearing capacity [19]. Therefore, a thorough understanding of the mechanical properties of fouled ballast is imperative in view of safety, stability and maintenance aspects.

According to Selig and Waters [39], ballast fouling can be contributed to two main categories: 1) the attrition or the breakdown of ballast particles, which accounts for up to 76% of deterioration within the ballast layer; 2) the contamination by the external substances, such as soils or muds from the substructure (i.e. subgrade and subballast), coal or fly ash infiltrating from the surface (i.e. falling off freight wagons), and the wear materials from concrete or timber sleepers. The fouling of ballast varies from place to place, and depends on various factors, such as the location and the specific use of the railway network. For example, railway tracks in desert areas are mainly fouled by wind-blown sands, while clay slurries are the main fouling agents for railways in low-lying floodplain regions. Along busy coal lines, fouling by coal dropping off wagons during passage of trains is very common.

Huang et al. [12] conducted direct shear tests on dry and wet fouled ballast and found that moisture content played a significant role in influencing the shear behavior of fouled ballast. Danesh et al. [5] investigated the influence of fouling materials on the shear behavior of railway ballast with different gradations by adding sand and clay fouling. An empirical equation was also established to quantify the role of the extent of fouling on the overall stress-strain behavior of the granular assembly. Much laboratory work has been carried out in the past to evaluate and quantify the strength and deformation properties of ballast contaminated by various fouling materials under both monotonic and cyclic loading conditions [43,15,35,24,14,8]. The influence of fouling fines on the drainage capacity of ballast assemblies has also been explored in the existing research [44,18,25].

During shearing of a granular mass, its quantitative stress-dilatancy relationship is considered to be an imperative indicator for interpreting the plastic deformation and corresponding stability. In a

well-known classical study, Rowe [36] introduced a stress-dilatancy equation by investigating the interplay of dilatancy and soil shear strength based on conventional triaxial testing as given by Eq. (1).

$$\frac{\sigma_1'}{\sigma_3'} = K\left(1 - \frac{d_{\varepsilon_v}^p}{d_{\varepsilon_1}^p}\right) \quad (1)$$

where σ_1' and σ_3' are the major and minor principal stresses, respectively; ε_v and ε_1 are the volumetric and axial strain, respectively; *K* is a dimensionless index related to the angle of shearing resistance of soils and also a function of the bulk modulus. More details of stress-dilatancy behavior of various soils are described elsewhere [1,46,41,42,30,10,47]. For instance, Dolzyk-Szypcio [7,6] found that the stress-dilatancy relationship for latite basalt is bilinear in triaxial compression tests, while Indraratna et al. [19] gives evidence of highly non-linear stress-dilatancy response for latite basalt (volcanic) at elevated applied stresses attributed to continual breakage in line with heavy haul loading. Sun et al. [40] proposed an elasto-plastic constitutive model to capture the stress-strain behavior incorporating ballast degradation. Indraratna et al. [17] investigated the stress-strain response of coal-fouled ballast at various confining pressures and developed a multiphase constitutive model by considering the fouling content in conjunction with particle breakage. SarojiniAmma et al. [37] established a semi-empirical dilatancy model for clay-fouled ballast and proposed three empirical constants depending on the fines content.

Despite significant progress made so far in constitutive modelling of granular media, comprehensive research on the stress-dilatancy relationships for coarse granular assemblies and in particular for fouled ballast posing considerable track stability is still limited in a fundamental view point. Due to the substantial diversity of physical properties of fouling materials, the implications on track behavior governed by fouling are broad and warrant specific studies in relation to given fouling agents without adopting generalized relationships. Besides, most of the aforementioned studies have been experimentally involved, and mainly macroscopic properties of fouled ballast have been

examined in detail. The pioneering work of Cundall and Strack [4] on the Discrete Element Method (DEM), provides an invaluable tool for understanding the microscopic properties of granular materials that has been successfully applied to both clean [2,29,26,9,28] and fouled ballast [16,32,33,13,11]. Considering the requirement for identifying the varied stress-dilatancy influences of two distinct fouling agents, a series of large-scale direct shear tests were conducted on coal-fouled and clay-fouled ballast aggregates in current research. In this study, corresponding numerical models were established in Particle Flow Code3D, PFC3D, with the key objective of providing greater insight to the performance of ballasted rail tracks.

2. Large-scale direct shear testing

The large-scale direct shear apparatus designed and built at Wuhan University can accommodate a test specimen of 600 mm (L)×600 mm (W)×500 mm (H), as shown in Fig. 1(a), with each of the shearing box being 250 mm high. The horizontal and vertical jacks are controlled by a servo-control system to apply the normal and shear loads to the specimens. A number of spherical bars having a diameter of 10 mm are placed under the bottom shearing box to reduce the contact area, and hence to minimise the base frictional resistance. Stress and strain are recorded by the linear variable differential transformers (LVDT) at regular intervals.

Ballast used in the research is crushed granite which is the most common material for ballasted railway tracks in China. The ballast was washed, dried and sieved to comply with the Chinese Railway Ballast Standard (TB/T 2140-2008), and clay and coal fines were chosen as the fouling materials. The size distributions of ballast aggregates and fouling materials are presented in Fig. 1(b). The engineering properties of ballast, coal and clay fines are listed in Table 1. Each specimen contains fresh ballast weighing 270 kilograms. The amount of fouling materials is quantified using the Void Contaminant

Index (VCI) proposed by Indraratna et al. [20] as given by

$$\mathrm{VCI} = \frac{1+e_f}{e_b} \times \frac{G_{s-b}}{G_{s-f}} \times \frac{M_f}{M_b} \times 100 \quad (2)$$

Where e_f, G_{s-f} and e_b, G_{s-b} are the void ratio and the specific gravity of fouling material and ballast aggregates as listed in Table 1. M_f and M_b are the dry mass of fouling materials and fresh ballast. In this study, coal-fouled and clay-fouled ballast aggregates were prepared at three different levels of VCIs, i.e. 0%, 20% and 40%. In practice, VCI=40% is considered to be a critical state for fresh ballast aggregates where urgent maintenance is needed. Therefore, only fouling levels under 40% are considered in the current research. The corresponding amount of coal and clay needed for each test specimen was determined according to Eq. 2. The fouling material was dried and mixed up with fresh ballast, after which the mixed aggregates were placed in the shearing box in five layers, with each layer being approximately 100 mm high. Then the specimens were pre-compacted under a normal pressure of 100 kPa so that the predetermined porosity (i.e. 0.43) could be reached. A total of 3 normal pressures (15, 35 and 55 kPa) were applied to the specimens, and they were maintained at a constant level during the shearing process by the servo-control system. The shearing rate was 3 mm/min, and all the specimens were sheared until a total shear displacement of 60 mm (i.e. 10% shear strain) was reached.

3. Discrete Element Modeling

Numerical modelling of fouled ballast was carried out using the DEM software, PFC3D. In this research, ballast particles are represented as irregularly-shaped clumps created using the method introduced by Chen et al. [3]. The shapes of clumps resemble the angularity of real ballast particles in the laboratory experiments as given in Fig. 2(a). Despite that the coal and clay fines also have irregular shapes and various particle sizes, but they are simplified as spheres in the current DEM analysis. The size distribution of coal particles is the same as that in the laboratory tests. As for clay fines, they have

a wider size distribution in the experiments, ranging from 0.01 mm to 15.50 mm. However, the time-step would be limited to an unacceptably low level if the sizes of particles are too small [23]. In this regard, the medium size value of clay particles, i.e. 1.2 mm, has been used as the typical representative diameter of flocculated clay particles in the PFC models. Note that dispersed clay grains are minute (microns) following molecular dynamics, and they cannot be properly analysed in the current DEM analysis. The linear contact model has been used for all the simulations. Table 2 lists the parameters used in the contact model.

To establish the model, a group of overlapped spheres with different sizes were firstly generated inside the shearing box of dimensions of 600 mm (L) × 600 mm (W) × 500 mm (H), thus replicating the exact laboratory condition. The overlapped spheres were then cycled to reach the equilibrium state where the unbalanced force ratio was less than $1e^{-5}$. The aforementioned ballast clumps as shown in Fig. 2(a) were used to replace the spheres with the same volumes at random, after which the voids of the skeleton were filled with small fouling grains (also spherical) using the subroutines developed by the authors. At this stage, the friction between bodies were set to zero in order to improve the density of the aggregates. A baffle wall was created in the middle of the shearing box and moved with the bottom box as shearing progressed.

Fig. 2(b) presents a typical diagram of coal-fouled sample with VCI of 20%. Around 4300 ballast clumps are generated in the model. The number of fouling spheres for VCI of 20% and 40% is 21610 and 43750 for coal fines, and 130225 and 260339 for clay fines, respectively. The initial specimens were compacted to a normal pressure of 100 kPa similar to the laboratory experiments. During the shearing process, the forces on the boundary walls were recorded and the normal and shear stresses were calculated according to Eq. 3 and Eq. 4, as given by

$$\sigma_n = \frac{N_{tw}}{L \times W} \tag{3}$$

$$\tau_s = \frac{N_{rw} + N_{lw} + S_{bw}}{(L - \text{vt}) \times W} \tag{4}$$

Where N_{tw}, N_{rw} and N_{lw} represent the normal forces acting on the top, right and left side wall, as shown in Fig. 2(c); S_{bw} is the shear force on the bottom wall; *L* and *W* are the dimension of the initial shearing box; *v* and *t* are the velocity (rate) and the time of shearing, respectively, and *v* was set to 0.005 mm/s as used in the laboratory experiments. During simulation, the movement of the top wall was controlled via a servo-control system to maintain a constant normal pressure [27].

4. Results and Discussion

4.1 Effect of normal stress on the shear behavior of ballast

The responses of shear stress (τ_s) and normal strain (ε_n) during shearing for clean and fouled ballast are presented in Fig. 3. Similar trends were observed for specimens under four different normal loadings. The shear stress τ_s increases at a declined gradient as the shear strain (ε_s) develops. The maximum τ_s for each specimen is reached when ε_s is at around 8%. As expected, the shear stress increases with the increase of normal pressure σ_n. This is primarily due to the enhanced interlocking between ballast particles under higher σ_n. However, the normal strain shows compressive behavior (negative value of ε_n). Subsequently, ε_n gradually increases with shearing and it decreases with the increase in σ_n. The results obtained by DEM simulations are also given in Fig. 3, and they indicate that the numerical models have captured the shear behavior similar to that of the experiments. The discrepancy of shear stress between laboratory tests and the corresponding numerical models becomes larger under higher values of σ_n. This is mainly due to the limitation of the current DEM model in capturing the breakage of ballast at higher σ_n.

4.2 Effect of fouling on the shear behavior of ballast

Fig. 4 shows the τ_s versus ε_s curves and ε_n versus ε_s plots for coal-fouled and clay-fouled ballast with different fouling levels at a normal stress of 55 kPa. With the increase of VCI, both coal-fouled and clay-fouled ballast experience decreasing shear stress and normal strain. Results from DEM simulations show similar trends as those of the laboratory experiment. Under the same fouling content (VCI), ballast fouled by clay fines exhibits larger shear stress and smaller normal strain than that of ballast fouled by coal fines. Notably, for the normal strain generated by 40%-VCI, DEM models indicate results that are slightly larger than 20%-VCI samples. This is not surprising given that at 40% VCI, the granular assembly is more likely to dilate given the less void space available for continual compression.

For coarse granular materials, the interlocking between particles can cause the shear resistance to be higher than those considering the inter-particulate friction only, which leads to the non-linearity of the Mohr-Coulomb strength envelope. It is also noteworthy that the any cohesion provided by the clay fines compared to typically cohesionless coal fines within the granular assembly is not modelled in this DEM analysis.

By conducting a series of large-scale triaxial tests on greywacke rock fills, Indraratna et al. [42] concluded that the relationship between normalized peak shear stress and normalized normal stress generally follows the power equation as given by Eq. 5.

$$\frac{\tau_p}{\sigma_c} = a\left(\frac{\sigma_n}{\sigma_c}\right)^b \tag{5}$$

In the above, τ_p is peak shear stress, σ_n is normal pressure, σ_c is strength of parent rock under uniaxial compression, and is set to be 130 MPa in the current research for replicating moderately weathered igneous rockfills such as granite, *a* and *b* are two dimensionless parameters which can be determined by non-linear regression. Fig. 5 shows the variation of normalized peak shear stress against

different normalized normal stress for both clean and fouled ballast aggregates. The fitting curves and the corresponding empirical parameters are also presented in Fig. 5. Clean ballast has the largest τ_p/σ_c values under all normalized normal stress. At VCI of 20%, τ_p/σ_c for clay-fouled ballast is greater than that for coal-fouled, which is probably due to the larger particle sizes of coal grains compared to clay fines. The relatively coarse coal fines may act as obstacles and reduces the ballast-ballast contact pressure, while clay fines mainly adhere to the ballast surface. These findings are consistent with the observations made by Huang et al. [12]. Moreover, τ_p/σ_c reduces to almost the same values for both coal-fouled and clay-fouled aggregates with 40% VCI. For highly-fouled ballast, the voids in skeleton are usually filled by external impurities and there is limited extra space for particle during shearing. The geometry and physical properties of fouling fines are no longer the predominant factors in influencing the behaviors of the ballast aggregates. This is also the crucial condition when urgent maintenance operations should be advocated as indicated by Selig and Waters [39].

Fig. 6 shows the peak dilatancy angle (ψ_m) of coal-fouled and clay-fouled ballast aggregates. As expected, ψ_m decreases with the increase of normal stress for both clean and fouled ballast. When it comes to the influence of VCI, it can be found that ψ_m decreases as VCI increases. Since the voids in the ballast skeleton are occupied by coal fines or clay fines, there is less space for ballast particles to move up and over their surrounding particles, resulting in a decrease of ψ_m. Besides, as clay fines have a wider size distribution than coal fines in the current research, the clay-fouled aggregates were denser than the coal-fouled ones at the same degree of fouling. Therefore, ballast fouled by coals has slightly larger ψ_m values compared to that fouled by clay fines, as shown in Fig. 6.

4.3 Stress-dilatancy behavior for fouled ballast

To study the stress-dilatancy relationship for fouled ballast, a non-linear model relating the stress

ratio (q/p) and the dilatancy ratio ($1-\frac{d\varepsilon_v^p}{d\varepsilon_1^p}$) was proposed by SarojiniAmma et al. [37] based on the experimental data from the large-scale shearing tests. The variations of stress ratio (τ_s/σ_n) versus dilatancy ratio ($1-\frac{d\varepsilon_v^p}{d\varepsilon_1^p}$) for clean and fouled ballast at various normal pressures were shown in Fig. 7. When the normal pressure increases from 15 kPa to 35 kPa, the dilatancy ratio of ballast aggregates is suppressed as shown in the Fig. 7. As σ_n increases to a higher value (i.e. 55 kPa), the stress-dilatancy curves would move to the left, indicating a lower volume change rate probably attributed to the breakage of ballast particles.

Fig. 8 shows the stress-dilatancy plots of ballast under various fouling conditions at σ_n=55 kPa. With the increase of VCI, both coal-fouled and clay-fouled ballast exhibit smaller stress ratios in line with smaller dilatancy ratios, as shown in Fig. 8(a) and Fig. 8(b). For 20%-VCI ballast, the clay-fouled samples show a higher stress ratio with a smaller dilatancy ratio compared to the coal-fouled samples (Fig. 8(c)); the stress ratio for ballast at 40%-VCI is nearly the same, while the clay-fouled ballast has a relatively smaller dilatancy ratio than coal-fouled ballast as shown in Fig. 8(d). This implies that coal fines introduce a greater detrimental effect on ballast than being fouled by clay fines in terms of the strength and volume deformation characteristics. Moreover, the DEM model also qualitatively captured the stress-dilatancy behavior similar to that of the laboratory experiments, as shown in Fig. 9.

4.3 Microscopic analysis using DEM models

4.3.1 Particle contacts

Fig. 10 presents the evolution of coordination number (*CN*) and the average contact force (F_{ave}) for coal-fouled and clay-fouled ballast under different fouling levels at normal pressure of 55 kPa. *CN* can be determined by Eq. 6 as introduced by O'Sullivan [34].

$$CN = \frac{2N_{tc}}{N_p} \quad (6)$$

where N_{tc} and N_p are the number of total contacts and the number of particles in aggregate. It can be seen from Fig. 10 that *CN* and F_{ave} are the largest for clean ballast and they decrease as VCI increases for both coal-fouled and clay-fouled ballast. This can be attributed to the particle 'coating effect' of fouling materials, as observed earlier by Indraratna et al. [16,15,22]. The *CN* of clay-fouled ballast is smaller than that of coal-fouled at all fouling levels, which can be contributed to the smaller particle sizes of clay fines and their potential adhesion to the ballast surface. For 20% clay-fouled ballast, the majority of contacts can still be maintained, therefore it has greater contact forces than 20% coal-fouled ballast. When VCI is at 40%, the infiltrated coal fines can strengthen the ballast skeleton by facilitating to form force chains within the granular mass, leading to an increase in the average contact force.

In order to quantify the anisotropy of contact force distribution for ballast aggregate, the contact force tensor f_{ij} was defined based on the fabric tensor, which was proposed earlier by Satake [38] with the aim of characterizing the distribution of particle contacts in the granular assembly. The contact force tensor f_{ij} is given by Eq. 7,

$$f_{ij} = \frac{1}{N_c F_t} \sum_{k=1}^{N_c} f_i^k f_j^k \quad (7)$$

where f_i^k is the contact force vector, F_t and N_c is the total force and the total number of contacts considered in the assembly, respectively. Three principal values, f_1, f_2 and f_3 ($f_1 > f_2 > f_3$) and the corresponding principal vectors can be determined considering the eigenvalues and the eigenvectors of the tensor [31]. The force concentration indicator β_1, which can be obtained with the first and the third principal value as given by Eq. 8, was proposed to quantify the distribution anisotropy of the vectors. The expression of β_1 is similar to the deviator fabric as proposed by Thornton [45], and a greater value of β_1 indicates the higher degree of force concentration.

$$\beta_1 = f_1 - f_3 \tag{8}$$

Fig. 11(a) shows the evolution of β_1 for ballast at σ_n of 55 kPa. It can be seen that β_1 is the largest at the initial stage of shearing as the aggregates are only subjected to normal loading; it decreases as shearing develops and attains its peak value when the peak shear strength of the assembly is reached. Compared to coal-fouled ballast, clay-fouled ballast has a larger β_1 value, resulting in a higher shear strength. The evolution of major principal force orientation θ_f, which is the angle between the major principal force vector and x-axis on XZ plane, is given in Fig. 11(b). As shown here, θ_f decreases from nearly 90° to around 25°, rotating the orientation of the major principal force from the vertical direction towards the horizontal plane. Additionally, the θ_f of clay-fouled ballast is larger than that of coal-fouled ballast at the same fouling level.

4.3.2 Particle movement

Fig. 12 shows the snapshots of ballast rotation for clean aggregate at σ_n=55 kPa. It should be clarified that particle rotation is zeroed before the shearing begins, and Fig. 12 represents the accumulative rotation during the entire shearing process. Most of particle rotation predominantly occurs within a band that develops from the rear upper box to the front of bottom box, as shown in Fig. 12(b). Three typical ballast particles in the rotation band are also presented Fig. 12. It is found that particles rotate counterclockwise, which in fact, is the pattern contrary to the shearing direction. Fig. 13 presents the number of ballast particles in terms of the rotation angle *E* at the end of shearing. Statistically speaking, more particles rotate at small Euler angles (*E* is around 5°) with the increase of VCI as shown in Fig. 13. This phenomenon indicates that fouling fines would facilitate the small particle rotations, which is known as the 'lubricant effect' as described by Indraratna et al. [16]. By comparison, the number of particles having large Euler angle decreases as VCI increases to 40%, which

contributes to the 'restraint effect' of fouling materials against the rotation of ballast particles. The mean value and the standard deviation of particle rotation for each specimen are also given in Fig. 13. As VCI increases, ballast aggregates exhibit a smaller average Euler angle with a lower standard deviation. In other words, particle rotation is impeded and more ballast particles rotate with smaller Euler angles with the increase of fouling materials, which also verifies that clay fines impose a greater restraint effect on the rotation of ballast particles than the coal fines.

Fig. 14(a) shows the velocity distribution of ballast particles for clean aggregates at ε_s of 10%, and there are generally four different movement patterns in a ballast assembly. Particles located at the rear region of the upper box mainly rotate around, while those at the bottom part of the box move horizontally or obliquely-downwards. The upward movement of ballast particles in the upper front accounts for the dilation of the aggregate and the average velocity of ballast particle in this region for coal-fouled and clay-fouled ballast at σ_n of 55 kPa is given in Fig. 14(b). With the increase of VCI, both coal-fouled and clay-fouled ballast show a decreasing average particle velocity, which verifies the 'restraint effect' of these fouling materials. Meanwhile, the coal-fouled ballast exhibits relatively larger velocities than those of the clay-fouled ballast, leading to a greater volume dilatancy ratio, as observed in the laboratory experiments.

5. Limitations of the study

1. Low applied stresses (< 55 kPa) on an igneous rockfill (granite) gives insignificant breakage, however, at much larger stresses that are more realistic for heavy haul trains (> 200 kPa), particle breakage will be significant and the current DEM model may deviate from accuracy.

2. While particle coating (lubrication) and restraining effects by fouling agents can be explained from the experimental data and to some extent from the DEM results, the additional cohesion provided by clay fines within the voids was not captured in the current analysis. The frictional effects within the voids provided by accumulated coal fines will be different to clay fines, and the DEM models are not yet advanced to capture these effects within the pore space.

3. Perfect matching of angularity of ballast particles is always a challenge, given the spherical particles that are clustered to replicate real life particles.

6. Conclusion

This paper investigated the stress-dilatancy behavior of ballast with two different fouling agents, whereby a series of large-scale direct shear tests was conducted on coal-fouled and clay-fouled ballast at various fouling levels. Corresponding numerical simulations were performed using the discrete element method (DEM). The micromechanical properties of ballast aggregates at various fouling conditions were analyzed, and the difference in influence between coal fines and clay fines on the ballast stress-strain response was explained from a discrete or particulate scale. On the basis of this DEM study, the following conclusions can be drawn:

1. As expected, the highest peak shear stress and the highest volumetric dilation were observed for clean ballast at all applied stress conditions, but they decreased with the increase of fouling level for both coal-fouled and clay-fouled ballast. Under the same fouling levels, coal-fouled ballast showed a more detrimental effect on the shear stress development and the accompanying deformation of the ballast assembly compared to the clay fines.

2. The relationship between the stress ratio and the dilatancy ratio can be well-captured by a second-order polynomial fitting. With the increase of VCI, ballast aggregates exhibit a lower stress ratio with a smaller volume dilatancy ratio. Under the same fouling level, clay-fouled ballast could reach a higher stress with a smaller dilatancy ratio than that of coal-fouled ballast.

3. Upon shearing, clean ballast exhibited the largest coordination number with the greatest average contact force. The addition of coal fines or clay fines seemed to have impeded the inter-particle contacts within the granular mass, hence reducing the average contact force within the granular assembly, and this could be attributed to the 'coating effect' of fouling material. Compared to clay-fouled ballast, the coal-fouled aggregate had greater coordination numbers at all fouling levels and smaller average contact forces at VCI of 20%. In contrast, the strengthening effect of the ballast skeleton provided by infiltrated coal fines at VCI of 40% facilitated the formation of strong force chains within the aggregate body, leading to an increased average contact force.

4. As shearing developed, the anisotropy of contact forces for ballast aggregate decreased and the major principal force gradually rotates from the vertical direction towards the horizontal plane. The DEM results showed that the clay-fouled ballast indicated larger force concentration and a greater major principal force rotation compared to the coal-fouled ballast.

5. Much of particle rotation was seen to be located within a distinct band in the proximity of the shearing plane. Due to the addition of fouling agents, the small particle rotations within the assembly were more easily facilitated, while the coarser particle rotations were relatively

more restrained. In general, ballast fouled by clay fines showed smaller rotations than the coal-fouled ballast.

6. The average particle velocity decreased with the increase in fouling level; the coal-fouled ballast exhibited larger velocities compared to clay-fouled ballast at the same fouling level.

Conflicts of Interest

The authors all declare no conflict of interest.

Acknowledgements

This work was financially supported by Chinese Scholarship Council (No. 201906270149); National Natural Science Foundation of China (NSFC) (Grant No. 51878521, 51178358) and the support of the ARC Industrial Transformation Training Centre, ITTC-Rail at the University of Wollongong. The support is gratefully acknowledged.

References

[1] Been, K., Jefferies, M.: Stress dilatancy in very loose sand. Canadian Geotechnical Journal 41(5), 972–989 (2004). DOI 10.1139/t04-038

[2] De Bono, J.P., McDowell, G.R.: Investigating the effects of particle shape on normal compression and over consolidation using DEM. Granular Matter 18(3) (2016). DOI 10.1007/s10035-016-0605-5

[3] Chen, J., Gao, R., Liu, Y.: Numerical study of particle morphology effect on the angle of repose for coarse assemblies using DEM. Advances in Materials Science and Engineering 2019, 1–15 (2019). DOI 10.1155/2019/8095267

[4] Cundall, P., Strack, O.: Discrete numerical model for granular assemblies. International Journal

of Rock Mechanics and Mining Sciences & Geomechanics Abstracts 16(4), 77 (1979). DOI 10.1016/0148-9062(79)91211-7

[5] Danesh, A., Palassi, M., Mirghasemi, A.A.: Effect of sand and clay fouling on the shear strength of railway ballast for different ballast gradations. Granular Matter 20(3) (2018). DOI 10.1007/s10035-018-0824-z

[6] Dołżyk-Szypcio, K.: Stress–dilatancy for crushed latite basalt. Studia Geotechnica et Mechanica 40(1), 6–10 (2018). DOI 10.2478/sgem-2018-0002

[7] Dołżyk-Szypcio, K.: Stress–dilatancy relationship for railway ballast. Studia Geotechnica et Mechanica 40(2), 79–85 (2018). DOI 10.2478/sgem-2018-0018

[8] Esmaeili, M., Aela, P., Hosseini, A.: Effect of moisture on performance of mixture of sand-fouled ballast and tire- derived aggregates under cyclic loading. Journal of Materials in Civil Engineering 31(2), 04018377 (2019). DOI 10.1061/(asce)mt.1943-5533.0002586

[9] Feng, B., Park, E.H., Huang, H., Li, W., Tutumluer, E., Hashash, Y.M., Bian, X.: Discrete element modeling of full-scale ballasted track dynamic responses from an innovative high-speed rail testing facility. Transportation Research Record: Journal of the Transportation Research Board 2673(9), 107–116 (2019). DOI 10.1177/0361198119846475

[10] Harehdasht, S.A., Karray, M., Hussien, M.N., Chekired, M.: Influence of particle size and gradation on the stress-dilatancy behavior of granular materials during drained triaxial compression. International Journal of Geomechanics 17(9), 04017077 (2017). DOI 10.1061/(asce)gm.1943-5622.0000951

[11] Huang, H., Tutumluer, E.: Discrete element modeling for fouled railroad ballast. Construction and Building Materials 25(8), 3306–3312 (2011). DOI 10.1016/j.conbuildmat.2011.03.019

[12] Huang, H., Tutumluer, E., Dombrow, W.: Laboratory characterization of fouled railroad ballast

behavior. Transportation Research Record: Journal of the Transportation Research Board 2117(1), 93–101 (2009). DOI 10.3141/2117-12

[13] Huang, H., Tutumluer, E., Hashash, Y.M.A., Ghaboussi, J.: Discrete element modeling of aggregate behavior in fouled railroad ballast. In: Recent Advancement in Soil Behavior, in Situ Test Methods, Pile Foundations, and Tunneling. American Society of Civil Engineers (2009). DOI 10.1061/41044(351)6

[14] Hudson, A., Watson, G., Pen, L.L., Powrie, W.: Remediation of mud pumping on a ballasted railway track. In: A. Correia (ed.) Advances in Transportation Geotechnics, vol. 143, pp. 1043–1050. 3rd International Conference on Transportation Geotechnics, Elsevier Science Bv, Guimaraes, Portugal (2012)

[15] Indraratna, B., Ngo, N.T., Rujikiatkamjorn, C.: Deformation of coal fouled ballast stabilized with geogrid under cyclic load. Journal of Geotechnical and Geoenvironmental Engineering 139(8), 1275–1289 (2013). DOI 10.1061/(asce)gt.1943- 5606.0000864

[16] Indraratna, B., Ngo, N.T., Rujikiatkamjorn, C., Vinod, J.S.: Behavior of fresh and fouled railway ballast subjected to direct shear testing: Discrete element simulation. International Journal of Geomechanics 14(1), 34–44 (2014). DOI 10.1061/(asce)gm.1943-5622.0000264

[17] Indraratna, B., Nimbalkar, S., Coop, M., Sloan, S.W.: A constitutive model for coal-fouled ballast capturing the effects of particle degradation. Computers and Geotechnics 61, 96–107 (2014). DOI 10.1016/j.compgeo.2014.05.003

[18] Indraratna, B., Nimbalkar, S.S., Tennakoon, N.: The behaviour of ballasted track foundations: Track drainage and geosynthetic reinforcement. In: GeoFlorida 2010. American Society of Civil Engineers (2010). DOI 10.1061/41095(365)241

[19] Indraratna, B., Salim, W., Rujikiatkamjorn, C.: Advanced Rail Geotechnology - Ballasted Track.

Taylor & Francis Ltd. (2011)

[20] Indraratna, B., Su, L.J., Rujikiatkamjorn, C.: A new parameter for classification and evaluation of railway ballast fouling. Canadian Geotechnical Journal 48(2), 322–326 (2011). DOI 10.1139/t10-066

[21] Indraratna, B., Wijewardena, L.S.S., Balasubramaniam, A.S.: Large-scale triaxial testing of grey wacke rockfill. Ge´otechnique 43(1), 37–51 (1993). DOI 10.1680/geot.1993.43.1.37

[22] Indraratna, B., Tennakoon, N., Nimbalkar, S., Rujikiatkamjorn, C.: Behaviour of clay-fouled ballast under drained triaxial testing. Ge´otechnique 63(5), 410–419 (2013). DOI 10.1680/geot.11.p.086

[23] Itasca: PFC3D 5.0 particle flow code in three dimensions, theory and implementation volume. Minneapolis, Minnesota (2015)

[24] Kashani, H.F., Ho, C.L., Hyslip, J.P.: Fouling and water content influence on the ballast deformation properties. Construction and Building Materials 190, 881–895 (2018). DOI 10.1016/j.conbuildmat.2018.09.058

[25] Koohmishi, M., Palassi, M.: Effect of gradation of aggregate and size of fouling materials on hydraulic conductivity of sand- fouled railway ballast. Construction and Building Materials 167, 514–523 (2018). DOI 10.1016/j.conbuildmat.2018.02.040

[26] Li, H., McDowell, G.R.: Discrete element modelling of under sleeper pads using a box test. Granular Matter 20(2) (2018). DOI 10.1007/s10035-018-0795-0

[27] Liu, Y., Gao, R., Chen, J.: Exploring the influence of sphericity on the mechanical behaviors of ballast particles subjected to direct shear. Granular Matter 21(4) (2019). DOI 10.1007/s10035-019-0943-1

[28] Lu, M., McDowell, G.R.: The importance of modelling ballast particle shape in the discrete

element method. Granular Matter 9(1-2), 69–80 (2006). DOI 10.1007/s10035-006-0021-3

[29] McDowell, G.R., De Bono, J.P.: On the micro mechanics of one-dimensional normal compression. Ge´otechnique 63(11), 895–908 (2013). DOI 10.1680/geot.12.p.041

[30] Mohamadi, M., Wan, R., Shen, Z.: An elastoplastic description of frictional destructuration in natural clays and shales. Acta Geotechnica 13(4), 911–924 (2017). DOI 10.1007/s11440-017-0585-6

[31] Ng, T.T.: Discrete element method simulations of the critical state of a granular material. International Journal of Geomechanics 9(5), 209–216 (2009). DOI 10.1061/(asce)1532-3641(2009)9:5(209)

[32] Ngo, N.T., Indraratna, B., Rujikiatkamjorn, C.: DEM simulation of the behaviour of geogrid stabilised ballast fouled with coal. Computers and Geotechnics 55, 224–231 (2014). DOI 10.1016/j.compgeo.2013.09.008

[33] Ngo, N.T., Indraratna, B., Rujikiatkamjorn, C.: Micromechanics-based investigation of fouled ballast using large-scale triaxial tests and discrete element modeling. Journal of Geotechnical and Geoenvironmental Engineering 143(2), 04016089 (2017). DOI 10.1061/(asce)gt.1943-5606.0001587

[34] O'Sullivan, C.: Particulate Discrete Element Modelling. Taylor & Francis Ltd (2011)

[35] Rohrman, A.K., Ho, C.L.: Effects of fouling containing plastic fines on abraded ballast strength and deformation properties. Transportation Geotechnics 21, 100278 (2019). DOI 10.1016/j.trgeo.2019.100278

[36] Rowe, P.: The stress-dilatancy relation for static equilibrium of an assembly of particles in contact. Proceedings of the Royal Society of London. Series A. Mathematical and Physical Sciences 269(1339), 500–527 (1962). DOI 10.1098/rspa.1962.0193

[37] SarojiniAmma, B.K., Indraratna, B., Vinod, J.S.: A semi-empirical dilatancy model for ballast fouled with plastic fines. Geomechanics and Geoengineering 14(1), 12–17 (2018). DOI

10.1080/17486025.2018.1476737

[38] Satake, M.: Fabric tensor in granular materials. In: P. Vermeer, H. Luger (eds.) Deformation and failure of granular materials, pp. 63–68. Balkema, Rotterdam, The Netherlands (1982)

[39] Selig, E., Waters, J.: Track Geotechnology and Substructure Management. Thomas Telford Publishing (1995)

[40] Sun, Q., Indraratna, B., Nimbalkar, S.: An elasto-plastic method for analysing the deformation of the railway ballast. Procedia Engineering 143, 954–960 (2016). DOI 10.1016/j.proeng.2016.06.082

[41] Sun, Y., Gao, Y., Chen, C.: Critical-state fractional model and its numerical scheme for isotropic granular soil considering state dependence. International Journal of Geomechanics 19(3), 04019001 (2019). DOI 10.1061/(asce)gm.1943-5622.0001353

[42] Sun, Y., Gao, Y., Shen, Y.: Mathematical aspect of the state-dependent stress–dilatancy of granular soil under triaxial loading. Ge´otechnique 69(2), 158–165 (2019). DOI 10.1680/jgeot.17.t.029

[43] Tennakoon, N., Indraratna, B.: Behaviour of clay-fouled ballast under cyclic loading. Ge´otechnique 64(6), 502–506 (2014). DOI 10.1680/geot.13.t.033

[44] Tennakoon, N., Indraratna, B., Rujikiatkamjorn, C., Nimbalkar, S., Neville, T.: The role of ballast-fouling characteristics on the drainage capacity of rail substructure. Geotechnical Testing Journal 35(4), 104107 (2012). DOI 10.1520/gtj104107

[45] Thornton, C.: Numerical simulations of deviatoric shear deformation of granular media. Ge´otechnique 50(1), 43–53 (2000). DOI 10.1680/geot.2000.50.1.43

[46] Tun, W.T., Sato, T., Saito, H., Kohgo, Y.: Mechanical properties and stress–dilatancy relationships of unsaturated soil under various cyclic loading conditions. Acta Geotechnica 15(7), 1799–1813 (2019). DOI 10.1007/s11440-019-00908-5

[47] Xiao, Y., Meng, M., Chen, Q., Nan, B.: Friction and dilatancy angles of granular soils incorporating effects of shearing modes. International Journal of Geomechanics 18(11), 06018027 (2018). DOI 10.1061/(asce)gm.1943-5622.0001289

Table 1: Engineering properties of materials

	Specific gravity	Bulk density (kg/m^3)	Void ratio	Water content (%)	C_u	C_c	Liquid limit (%)	Plastic limit (%)
Ballast	2.66	1432	0.858	—	1.15	1.75	—	—
Clays	2.70	1178	1.207	22.2	15.50	0.91	42.10	22.40
Coals	1.22	715	0.707	—	1.59	1.17	—	—

Table 2: Parameters for contact models in DEM simulations

	Ballast	Coals	Clays
Particle density (kg/m^3)	2660	1220	2700
Contact stiffness of particle, $k_{\mathrm{np}}/k_{\mathrm{sp}}$ (N/m)	5.2×10^6	8.5×10^5	3.2×10^5
Contact stiffness of particle-wall, $k_{\mathrm{np-w}}/k_{\mathrm{sp-w}}$ (N/m)	1.0×10^7	1.0×10^7	1.0×10^7
Friction coefficient, μ_s	0.7	0.3	0.2

List of Figures and Tables

Fig. 13. Histograms of particle amounts with various rotation angle for (a) coal-fouled ballast and (b) clay-fouled ballast

Fig. 14. (a) The velocities of ballast particles at ε_s of 10% for clean ballast aggregate and (b) the average velocity of ballast particles for fouled aggregates

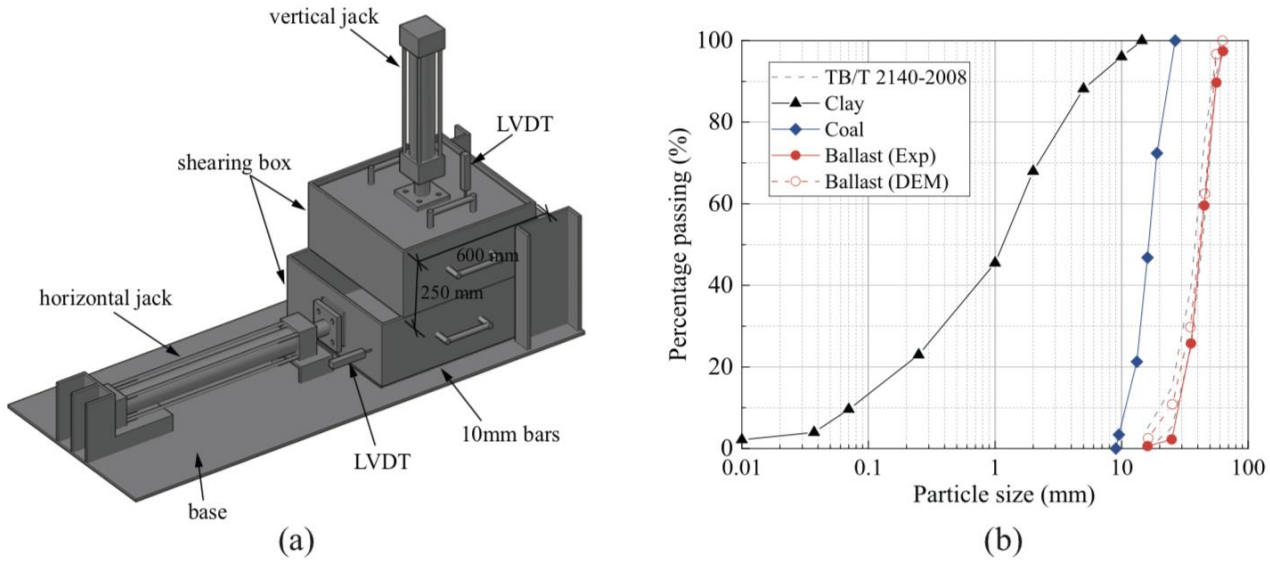

Fig. 1. Large-scale direct shear test: (a) schematic illustration of the apparatus and (b) size distribution of materials

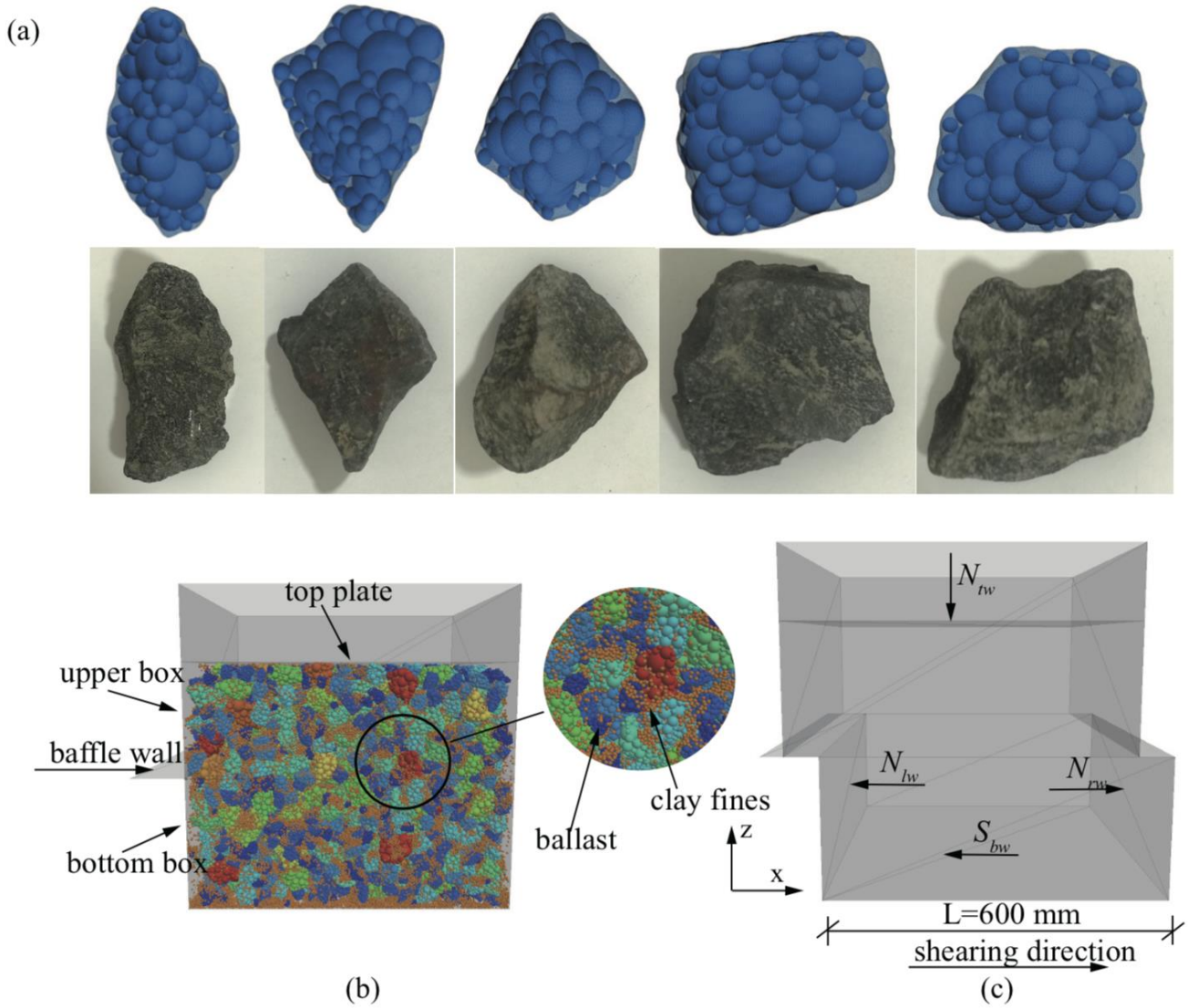

Fig. 2. DEM models: (a) ballast templates in PFC; (b) 20% clay-fouled sample and (c) schematic diagram of direct shear box

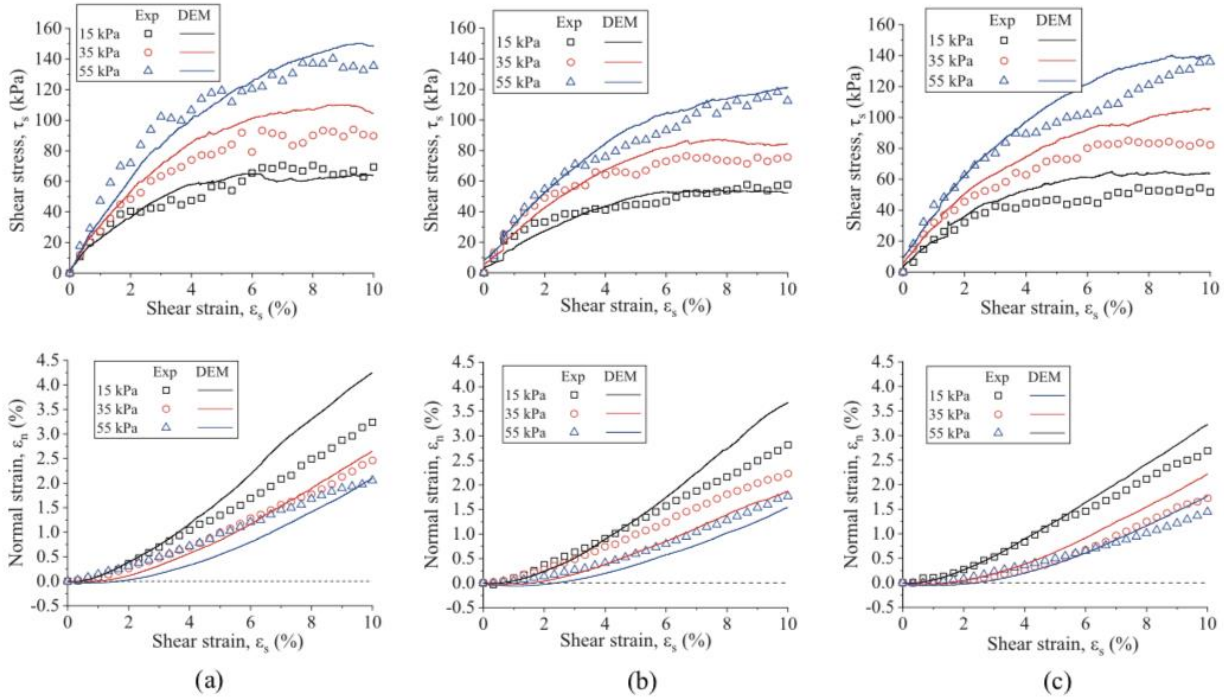

Fig. 3. Shear stress and deformation characteristics of: (a) clean ballast; (b) 20% coal-fouled ballast and (c) 20% clay-fouled ballast

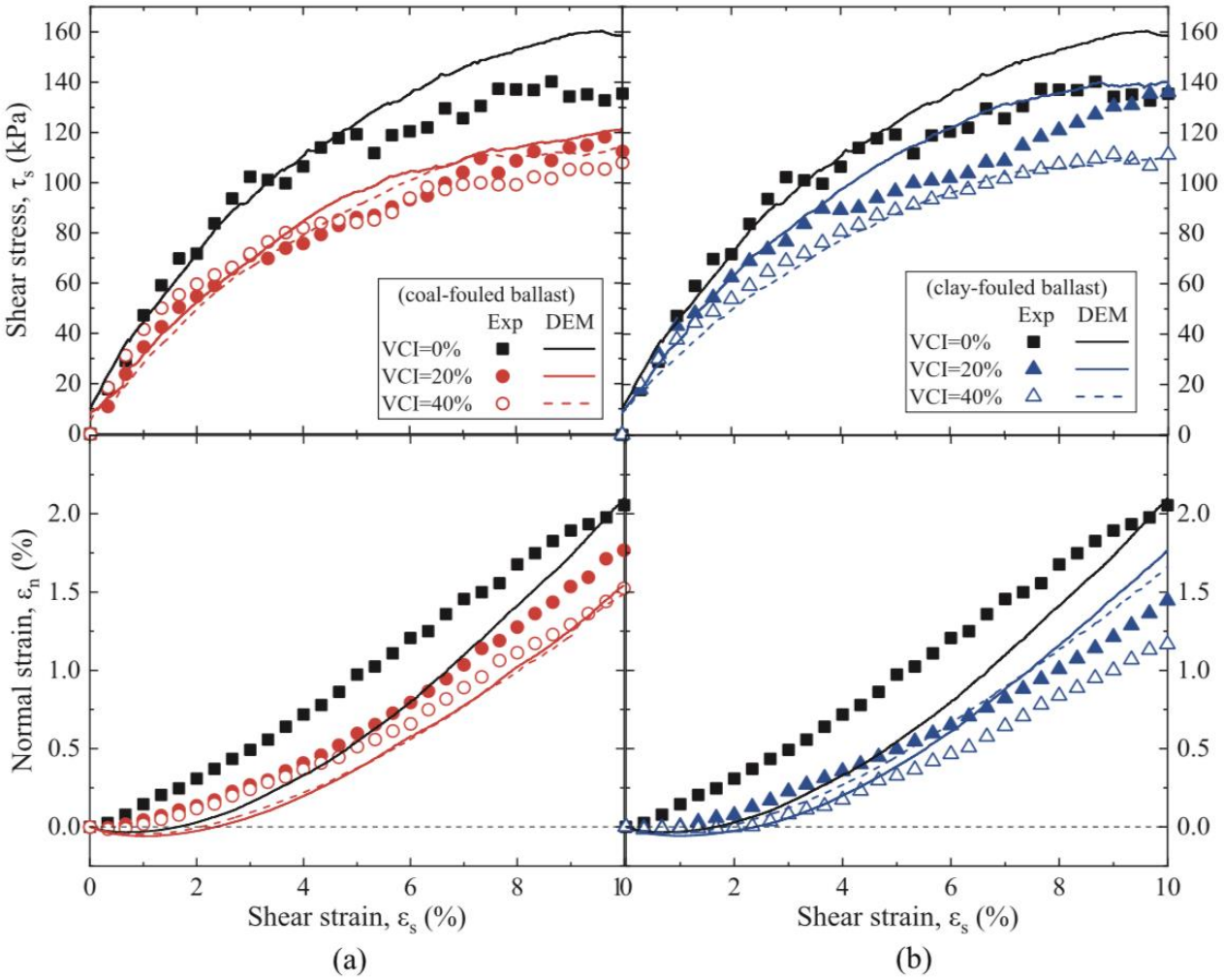

Fig. 4. Evolutions of shear stress and normal strain for ballast with various fouling VCI at σ_n of 55 kPa: (a) coal-fouled and (b) clay-fouled ballast

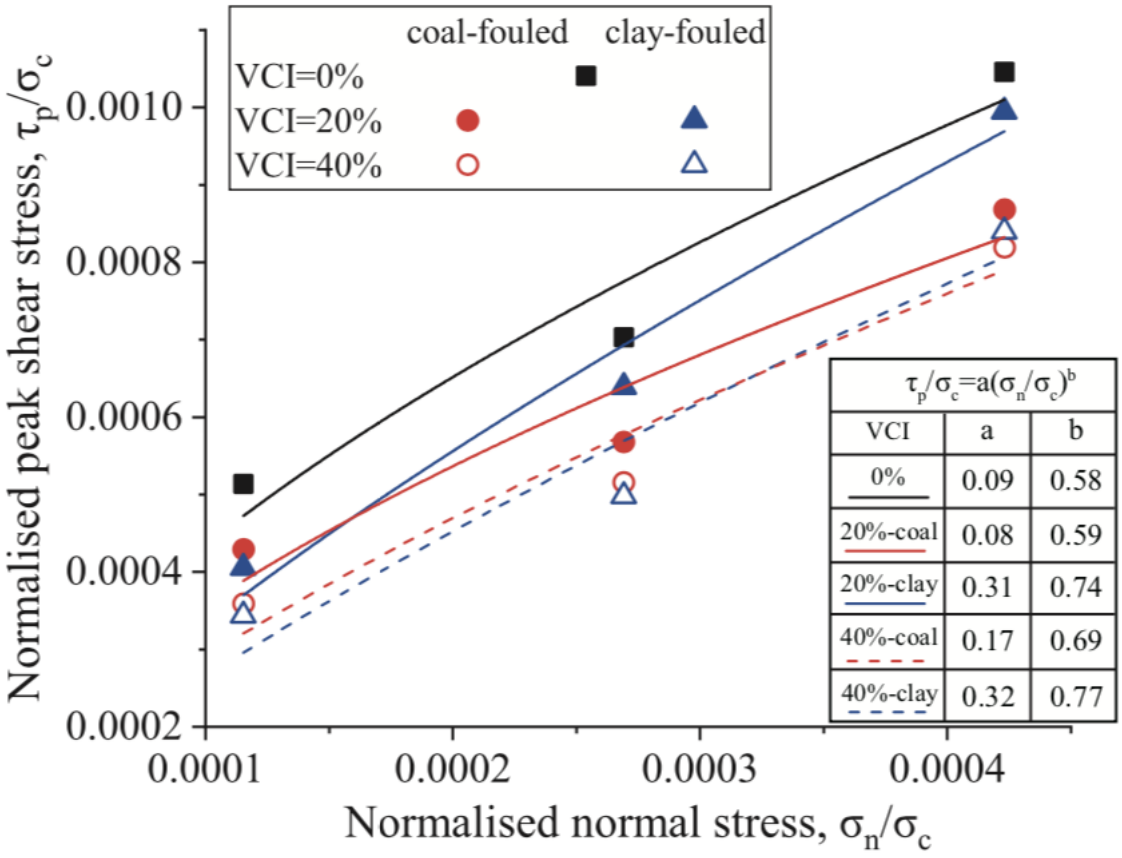

48

49 Fig. 5. The strength envelops for clean and fouled ballast under various fouling conditions

50

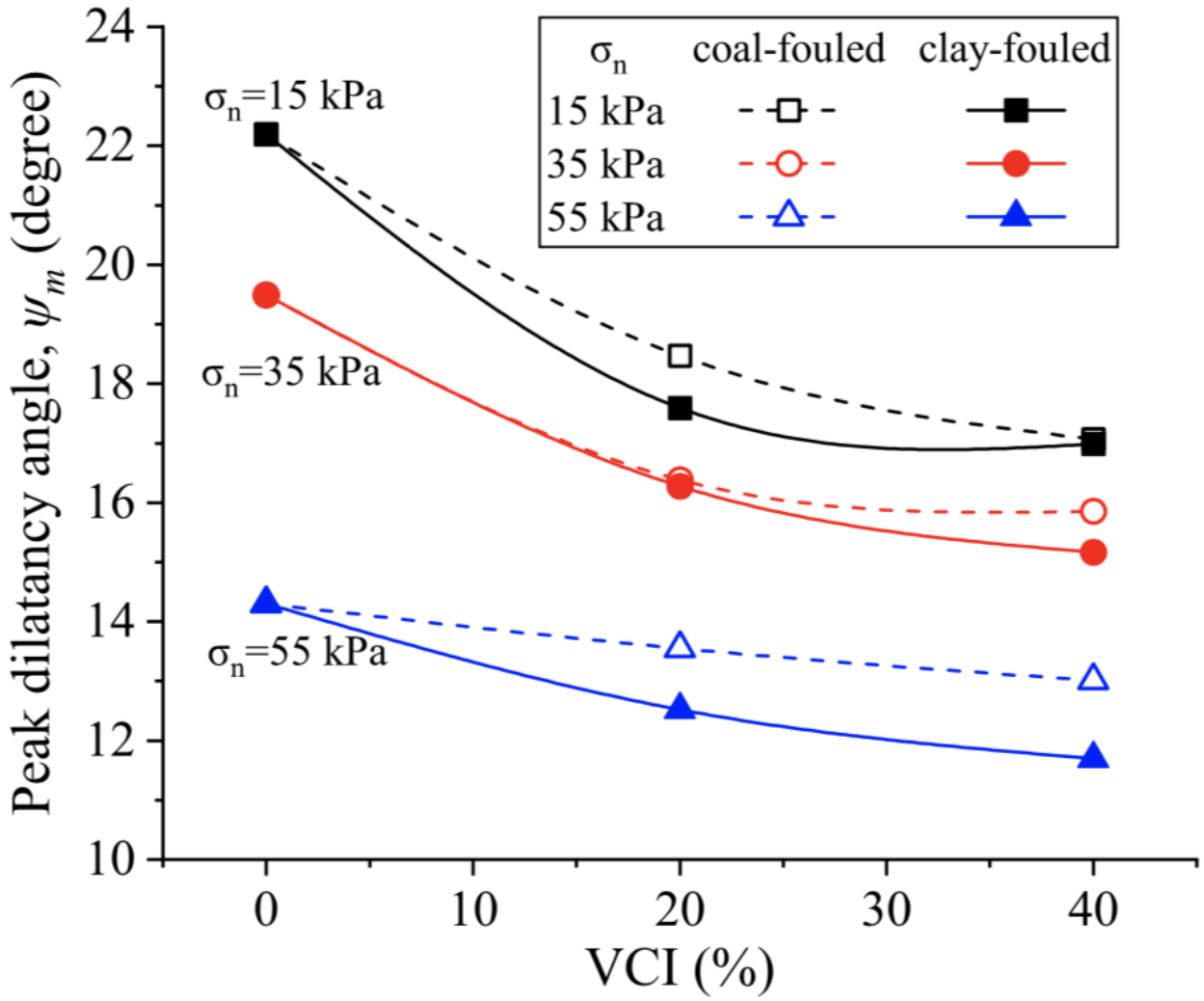

Fig. 6. The peak dilatancy angle for clean and fouled ballast under various fouling conditions

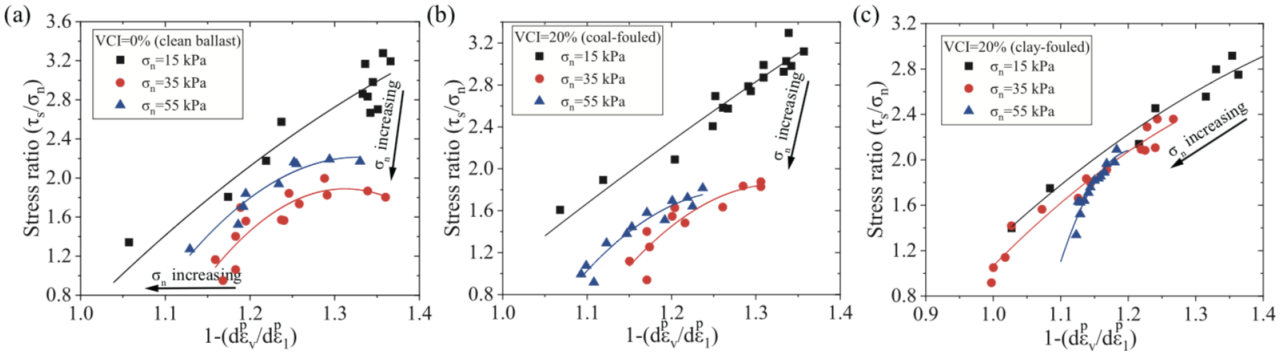

Fig. 7. Stress- dilatancy relationship for different normal stress: (a) clean ballast; (b) 20% coal-fouled ballast and (c) 20% clay-fouled ballast

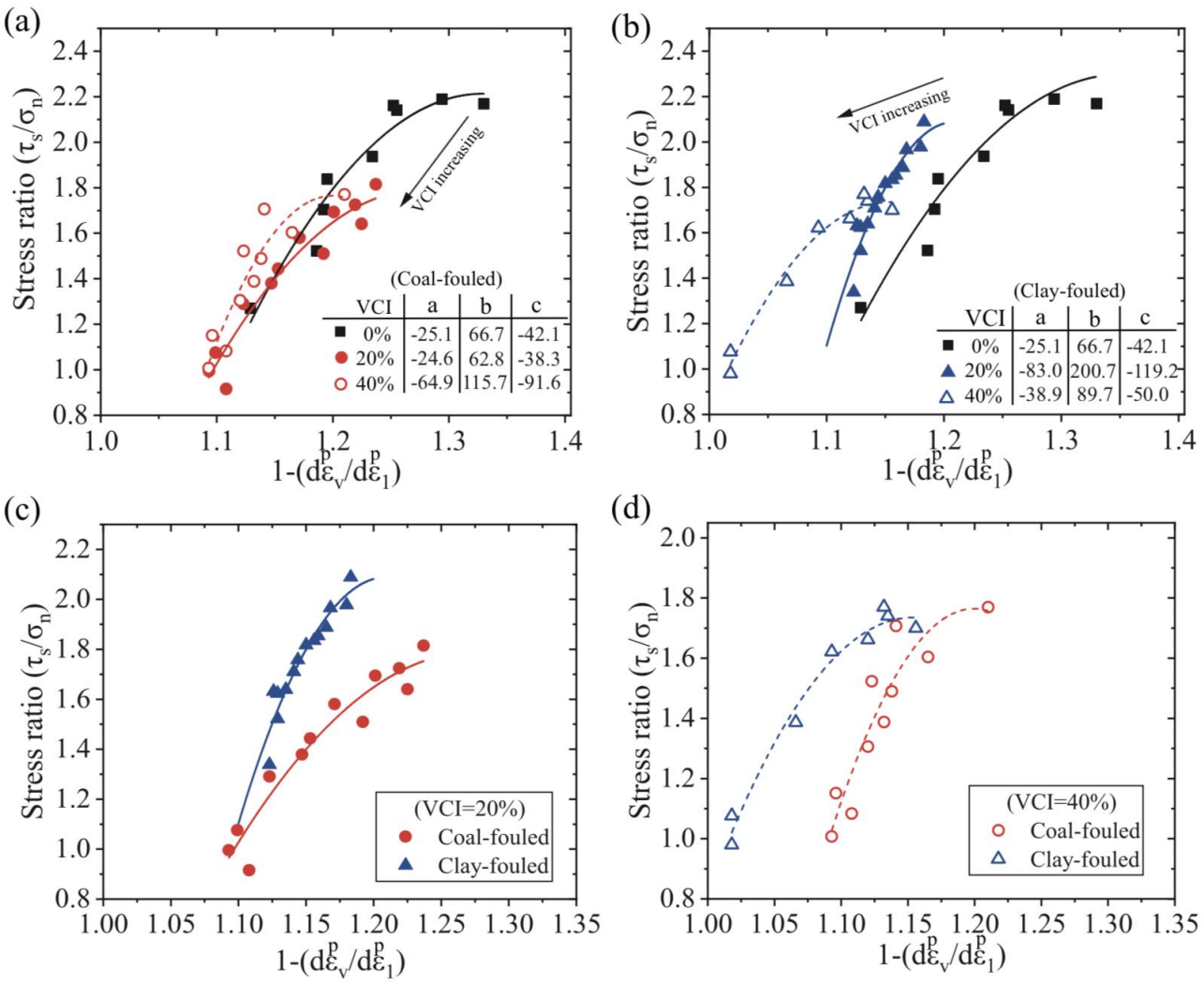

Fig. 8. Stress- dilatancy relationship for different fouling conditions at σ_n of 55 kPa: (a) coal-fouled ballast; (b) clay-fouled ballast; (c) 20%-fouled ballast and (d) 40%-fouled ballast

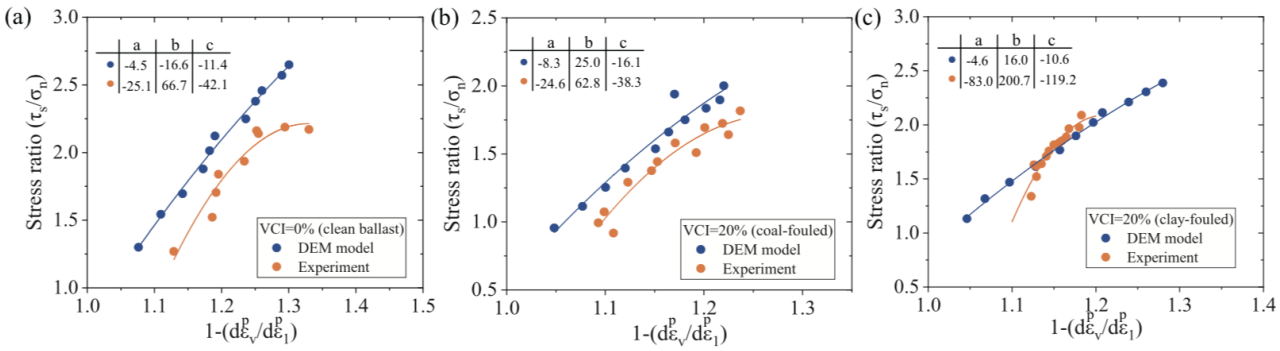

Fig. 9. Comparison of Stress- dilatancy relationship between DEM simulation and experiment at σ_n of 55 kPa: (a) clean ballast; (b) 20% coal-fouled ballast and (c) 20% clay-fouled ballast

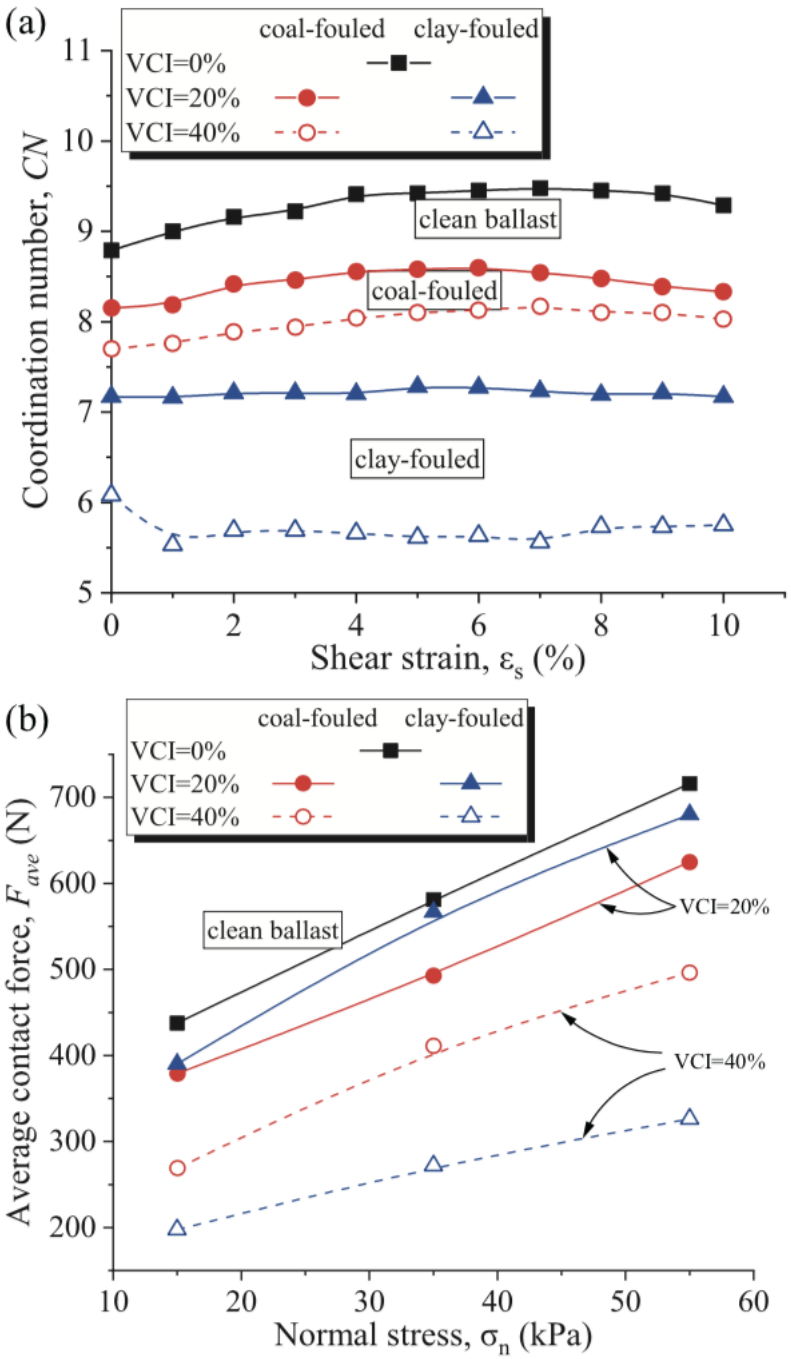

Fig. 10. The evolution of (a) coordination number and (b) average contact force for ballast aggregates

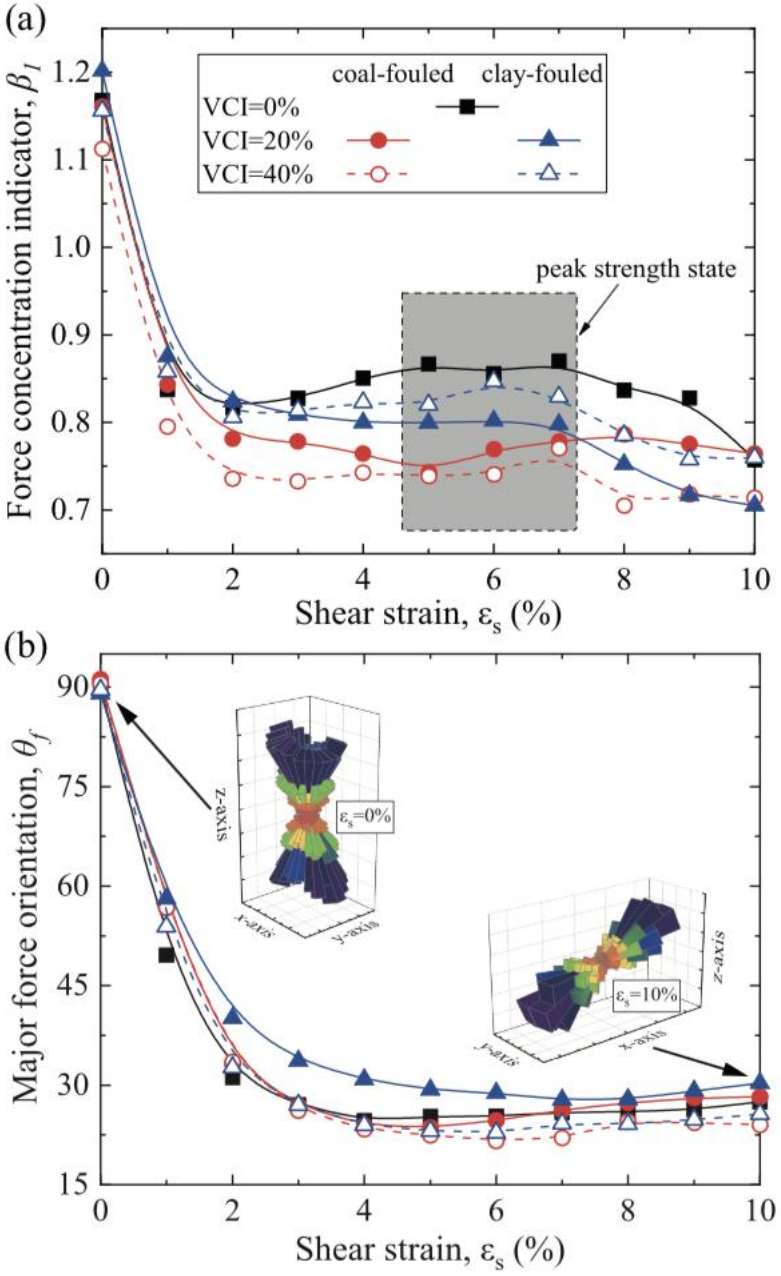

69

70 Fig. 11. The evolution of contact forces for ballast in terms of (a) force concentration indicator and (b)

71 major principal force orientation angle

72

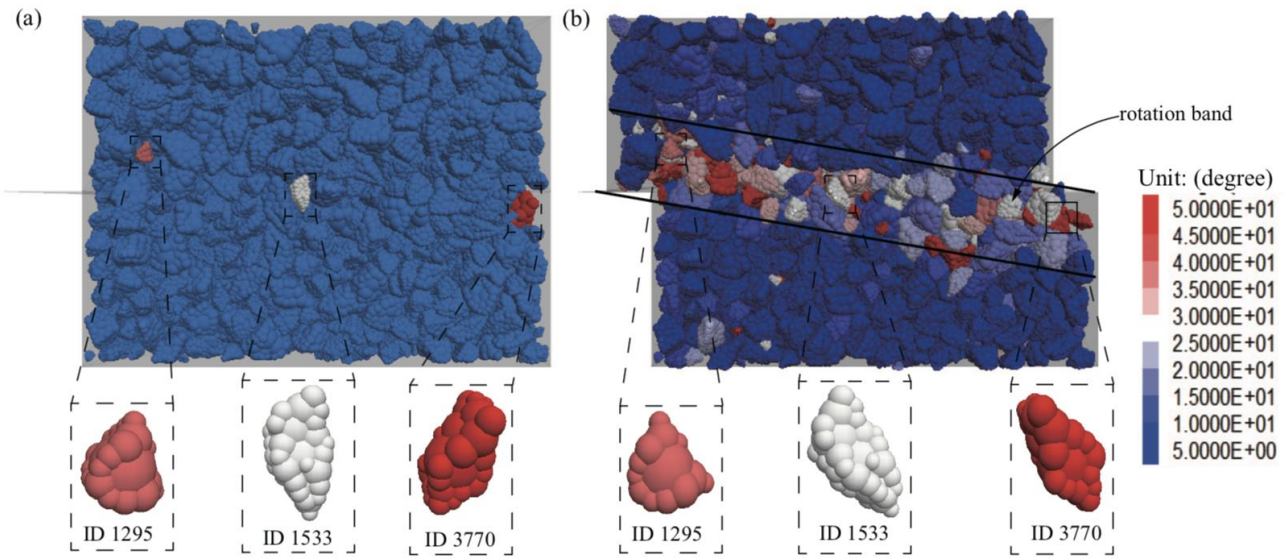

73

74 Fig. 12. The snapshot of ballast rotation for clean aggregate at ε_s of (a) 0% and (b) 10%

75

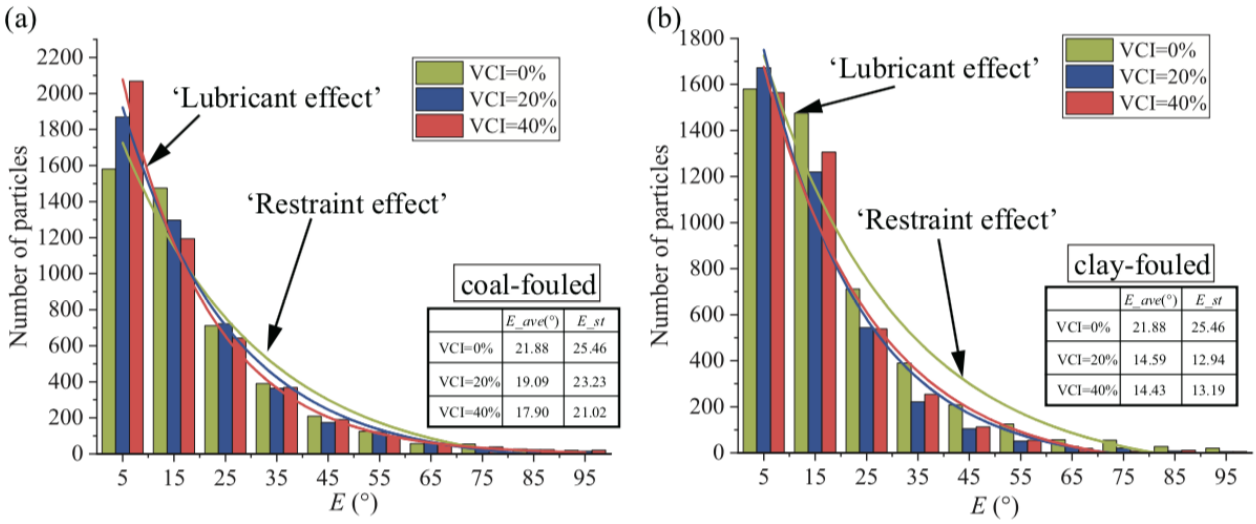

Fig. 13. Histograms of particle amounts with various rotation angle for (a) coal-fouled ballast and (b) clay-fouled ballast

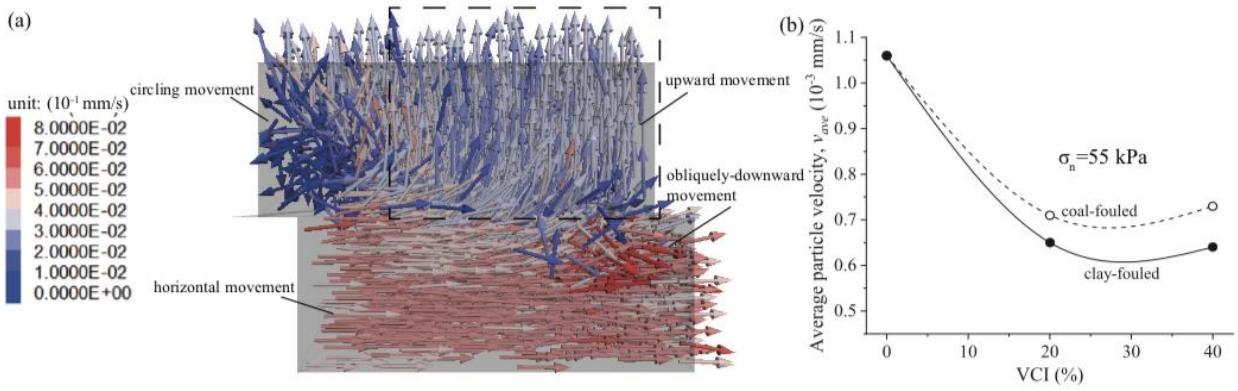

Fig. 14. (a) The velocities of ballast particles at ε_s of 10% for clean ballast aggregate and (b) the average velocity of ballast particles for fouled aggregates